RESEARCH ARTICLE

ADVANCED MATERIALS
www.advmat.de

Eco-Friendly Multifunctional Hydrogel Sensors Enabled Sustainable and Accurate Human-Machine Interaction System

Yanlong Zhao, Rui Wu, Yilin Hao, Yi Zhao, Xichong Zhang, Hui Liu, Wei Zhai, Kun Dai,* Caofeng Pan,* Chuntai Liu, and Changyu Shen*

Wearable epidermic electronics assembled by conductive hydrogels exhibit great application potential for their seamless integration with the human body for human-machine interactions (HMI). However, most multifunctional hydrogel sensors are prone to water loss and become useless e-waste, resulting in a growing threat to the global environment and human health. Inspired by the resurrection plants, this paper introduces the reversible intermolecular forces and physical crosslinking method into the hydrogel system to obtain a fully recyclable multifunctional smart hydrogel sensor (RMSHS), which can be completely recycled in a simple step. Meanwhile, RMSHS possesses admirable biocompatibility, excellent antibacterial ability (*S. aureus* and *E. coli* bacterial inhibition rate of 99.8%), rapid self-healing ability, and outstanding sensing performances such as low detection limit, fast response/recovery time (160/200 ms). Intelligent medical rehabilitation and smart HMI systems are developed for medical diagnostics and real-time remote controlling. Moreover, the recyclable triboelectric nanogenerator (R-TENG) intelligent array, designed based on RMSHS, replaces the electrode consumables in traditional TENGs, realizing the generation of green energy and 100% recyclability of electrode materials. RMSHS can be generalized and applied to other remote-controlling platforms, paving the way for large-scale, multi-scenario applications.

1. Introduction

Artificial intelligence (AI), big data, and virtual reality technology have exploded in recent years. Hydrogels, as the medium of human-machine interactions (HMI), have drawn intensive attention due to their adjustable functionality.[1] Hydrogels-based electronic devices can obtain different functions such as self-healing,[2] toughness,[3] antibacterial,[4] and biocompatibility by chemical modification or adding functional fillers. These adjustable functions make hydrogels have great potential aspects in the fields of biomedicine,[5] rehabilitation engineering,[6] electronic skin,[7] and intelligent robotics.[8] Especially, in the process of clinical rehabilitation treatment, a lot of repeated training is necessary for patients to recover, which often requires the accompaniment of medical staff, resulting in a burden on the medical staff.[9] Meanwhile, traditional electronic sensors have many drawbacks, which do not allow users to connect with electronic devices to achieve unique HMI.[10] The ideal medium with softness for comfort, self-healing for long service life, stable strain sensing for signal transmission, biocompatibility, and antibacterial properties for user safety to be used for HMI is urgently needed.[11] Another important factor in limiting the large-scale applications of hydrogel electronic sensors is that most hydrogel electronic sensors will lose their excellent performance due to water loss, resulting in a large amount of electronic waste, which causes great harm to nature and the

---

Y. Zhao, R. Wu, Y. Zhao, H. Liu, W. Zhai, K. Dai, C. Liu, C. Shen
School of Materials Science and Engineering
Key Laboratory of Materials Processing and Mold (Zhengzhou University), Ministry of Education
Zhengzhou University
Zhengzhou 450001, P. R. China
E-mail: weizhai@zzu.edu.cn; kundai@zzu.edu.cn

Y. Zhao, C. Pan
Institute of Atomic Manufacturing
Beihang University
Beijing 100191, P. R. China
E-mail: pancaofeng@buaa.edu.cn

Y. Hao
Advanced Intelligent Manufacturing Lab Nano Opto-mechatronics and Biomedical Engineering Lab (AIM-NOBE Lab) (Zhengzhou University)
Ministry of Education
Zhengzhou University
Zhengzhou 450001, P. R. China

X. Zhang
School of Computer Science and Technology
University of Science and Technology of China
Hefei, P. R. China

The ORCID identification number(s) for the author(s) of this article can be found under https://doi.org/10.1002/adma.202507127

DOI: 10.1002/adma.202507127

human body.[12] Therefore, the next-generation hydrogel-based HMI medium should consider its recyclability as well as its versatility.

PVA is of biocompatibility and non-toxicity, which can be broken down by penicillium and aspergillus in nature.[13] Quaternary ammonium chitosan (QCS) possesses a high solubility and a broad-spectrum bactericidal ability.[14] The involvement of active nanoparticles has been demonstrated to be an efficient method to impart multifunctional abilities to the hydrogels. Carbon quantum dots (CQDs) have attracted more and more attention for their biocompatibility, simple preparation, tunable structure, and functional properties.[15] However, various chemical initiators or harsh conditions are required during the fabrication of hydrogels, which are environmentally unfriendly or even toxic.[16] Moreover, most hydrogel-based sensors, enhancing the toughness by covalent bonding, cannot be recyclable or self-healing, which extremely limits the reusability and service time of hydrogel-based electronics. Meanwhile, most recyclable hydrogels have the problem that they can only be partially recovered, or the recycling process is complicated or most of the self-healing conductive hydrogels often have the defects of strong hysteresis. Therefore, it is still a huge challenge to fabricate conductive hydrogels with exceptional biocompatibility, low latency, rapid self-healing ability, and a simple recycling process.

Here, we develop a recyclable multifunctional smart hydrogel sensor (RMSHS), which is suitable for HMI scenarios in the future. The bioinspired RMSHS is designed by introducing reversible intermolecular forces, dynamic covalent bonds, and reversible physical crosslinking methods into the hydrogel system. RMSHS possesses fantastic recyclability (the hydrogels after the water loss can be 100% recycled), good antibacterial properties (bacterial inhibition rate of 99.8%), low dissipation energy (more than 81% of the maximum stress could be maintained under 0–150% strain after 100 cycles), and the rapid self-healing ability. Meanwhile, RMSHS possesses good sensing performances such as a low detection limit (1%), fast response/recovery ability (160/200 ms), and exceptional durability and stability. The RMSHS with excellent abilities enables people to realize real-time interaction with the machine through small movements of the fingers. We further combine rehabilitation robots with HMI technology, which allows patients to zealously participate in rehabilitation training. Meanwhile, doctors can diagnose and provide suggestions to patients remotely, which effectively reduces the burden on medical staff and saves medical resources. The intelligent remote gesture-controlling system can also be applied to other platforms, such as drones and cars. Moreover, RMSHS can be used as a stretchable electrode material to make a sustainable triboelectric nanogenerator (TENG), which further reduces the e-waste generated by electrode damage. This study proposes a novel and efficient device for the design of the ideal sustainable HMI medium.

2. Result and Discussion

2.1. Preparation and Characterization of RMSHS

In this study, the strategy of introducing the reversible intermolecular force-hydrogen bonds,[17] dynamic covalent bond-borate lipid bonds,[18] and reversible physical crosslinking method into the hydrogel system is employed to fabricate the recyclable multifunctional hydrogel.[19] PVA and QCS are employed as polymer chains, which possess abundant hydroxyl groups. The modified nitrogen-doped carbon quantum dots (N-CQDs) are achieved via a melting process under stage heating (Figure S1, Supporting Information).[20] N-CQDs are ellipsoidal (Figure S2a, Supporting Information) and the mean size of N-CQDs is about 2.5 nm (Figure S2b, Supporting Information). As shown in Figure S3 (Supporting Information), the FTIR absorption peak at 1649 cm^{-1} is related to the specific stretching vibration of C═O in N-CQDs. The two peaks at 1562 and 1124 cm^{-1} are attributed to the bending vibration of N-H and the stretching vibration of C-N-C, respectively. The FTIR broad absorption peak at 3420 and 3272 cm^{-1} are related to the stretching vibration absorption of -NH_2 and -OH, confirming the existence of abundant hydrophilic groups of hydroxyl and amino in N-CQDs.[21] XPS spectra are employed for analysis (Figure S4a, Supporting Information), the element peaks of C 1s, N 1s, O 1s, and S 2p are identified, and the high-resolution C 1s, N 1s, and O 1s spectra are also verified (Figure S4b–d, Supporting Information). The results of the XPS analysis are consistent with the FTIR, which confirms the doping effect of N and the abundant functional groups in N-CQDs. Due to the presence of hydrophilic groups hydroxyl and amino, the N-CQDs can be integrated into the water to form a uniform and transparent solution (Figure S5a,b, Supporting Information).

The preparation process of RMSHS is shown in Figure S6 (Supporting Information). The amino and the hydroxyl groups on the N-CQDs can interact with QCS and PVA chains to form hydrogen bonds. Borax acts as a crosslinking agent between PVA and QCS chains, which helps to generate dynamic borate esters (Figure S7, Supporting Information). The 3D cross-network structure is further developed through freezing and thawing. We can see from Figure S8a (Supporting Information), during the freezing process, the formation of ice crystals compresses the PVA molecular chains, bringing them closer together and thereby forming the "hard" hydrogen bonds regions of PVA crystalline. After multiple freeze-thaw cycles, the stable PVA crystalline microdomains are formed (Figure S8b, Supporting Information), which contain a large number of inter/intrachain hydrogen bonds, serve as crosslinking points to obtain robust hydrogel materials. In Figure S9a,b (Supporting Information), the microstructure of RMSHS confirms the formation of a robust cross-linked network. Moreover, as shown in Figure S10a,b (Supporting Information), the physical images further demonstrate the formation of the hydrogel. Infrared spectroscopy is employed, and the hydrogels fabricated with different contents, PVA/QCS/N-CQDs/Borax, PVA/QCS/Borax, and PVA/Borax are defined as PQCB, PQB, and PB. As shown in Figure S11a (Supporting Information), the strong and broad absorption peaks at around 3347 cm^{-1} of the PQCB are related to the stretching vibration of -OH and -NH_2.[22] The asymmetric stretching of B-O-C from the complexes shows discernible absorption peaks at 1321 and 1421 cm^{-1}. The characteristic peaks at 2938, 1654, and 1097 cm^{-1} are attributed to CH- asymmetric stretching, C═O carbonyl stretching, and CO- stretching, respectively.[23] Compared with the PB hydrogel in Figure S11b (Supporting Information), the increase in intensity of the absorption peaks at 1567 cm^{-1} is related to the bending vibration of the N-H. The intensity of the absorption peak at around 3347 cm^{-1} observably increases, indicating strong intermolecular hydrogen bonds in PQCB. FTIR results confirm that the addition of N-CQDs and QCS enhances the interaction in the hydrogels.

X-ray photoelectron spectra (XPS) measurements are employed to further discuss the internal interactions of PQCB, (Figure S12a–c, Supporting Information). Compared with the PB film, the new Cl element appears in the PQB and PQCB films, where the atomic percentages are 1.06 and 1.10 respectively, and the new N elements are 2.58 and 3.11, respectively.[24] Compared with PQB and PQCB hydrogel, the binding energy of N in XPS of N-CQDs shows a significant shift (Figure S13, Supporting Information), further substantiating the hydrogen bonding between PVA chains, N-CQDs, and QCS chains in the PQCB hydrogel. The energy-dispersive X-ray spectroscopy elemental mapping is employed (Figure S14, Supporting Information), exhibiting that the main elements (C, O, N, and Cl) in the hydrogel are distributed uniformly. Figures S12a and S14 (Supporting Information) demonstrate the uniform distribution of chlorine elements both on the surface and within the PQCB hydrogel matrix. The chlorine element in PQCB comes from QCS, and when QCS is dissolved in an aqueous solution, it will decompose into cationic ions, while the chlorine element exists in the form of ions in PQCB, which greatly increases electrical conductivity of PQCB. Moreover, PVA, QCS, and N-CQDs enable RMSHS to have better biocompatibility and antibacterial properties (**Figure 1**a). Furthermore, RMSHS shows great potential for intelligent HMI systems such as rehabilitation training (Figure 1b) and remote controlling like drones (Figure 1c). Benefiting from the design of a reversible hydrogel system, RMSHS discarded due to water loss can be 100% reused after a simple resurrection process like resurrected plants, without generating a large amount of e-waste (Figure 1d).

To optimize the mechanical properties of the RMSHS, the influence of N-CQDs content, the mass ratio percentage of QCS to PVA, and the mass ratio percentage of borax to the total mass of PVA and QCS are investigated in detail. The hydrogels without N-CQDs are defined as PQ_xB_y (x represents the mass ratio of QCS to PVA, and y represents the mass ratio of borax to the total mass of QCS and PVA). The Young's modulus (E), breaking strain (ε_b), and breaking strength (σ_b) of the PQB hydrogels is considered and the optimal ratio of gel content is explored in detail. For the PQB hydrogels, the increase of the mass ratio of QCS to PVA will result in high cross-linking density, endowing the PQB with high E and σ_b but low ε_b (**Figure 2**a; Figure S15a–c, Supporting Information). Simultaneously, an obvious toughening of the PQB is noticed when increasing the content of borax in the range of mass ratio 0.5-1.5. However, when the mass ratio percentage exceeds 1.5, the PQB becomes brittle because of the abundant borate ester bonds formed between molecular chains and the dense polymer network (Figure 2b; Figure S16a–c, Supporting Information). In summary, the $PQ_{40}B_{1.5}$ with outstanding mechanical properties (σ_b of 37 kPa and ε_b of 429%) will be used for further synthesizing with N-CQDs to fabricate RMSHS. When the N-CQDs content is low, the toughness of the hydrogel slightly reduces; while increasing the content of N-CQDs, it exhibits a reinforcement effect on the mechanical property of the PQCB. The E and σ_b of the PQCB rise from 9.9 and 33.6 kPa to 21.5 and 58.9 kPa (Figure S17a–c, Supporting Information), indicating that the combination of N-CQDs increases the mechanical strength of PQCB by forming more hydrogen bonds, thus providing a strong ability to disperse stress. In the meantime, the abundant hydroxyl and amino groups in N-CQDs can form more hydrogen bonds with molecular chains, endowing the PQCB with self-healing ability. PQCB hydrogels with different N-CQDs contents exhibit varying mechanical properties after three hours of self-healing. As shown in Figure 2d and Figure S18 (Supporting Information), the $PQ_{40}C_5B_{1.5}$ hydrogel self-healed for three hours demonstrates the best mechanical performance, with a maximum σ_b of 14.4 kPa and a maximum ε_b of 351%. In contrast, $PQ_{40}C_{50}B_{1.5}$ hydrogels self-healed for three hours exhibit a significant decrease in self-healing ability due to the excessive N-CQDs concentrations (Minimum σ_b of 1 kPa and a minimum ε_b of 27%). The effect of freeze-thaw times on the mechanical properties and self-healing properties of PQCB is also discussed. As can be seen from Figure 2d and Figure S19 (Supporting Information), when the freeze-thaw times exceed three times, its σ_b increases sharply and its modulus can reach 85.9 kPa, but its fracture strain decreases dramatically. At the same time, after the freeze-thaw times exceeded three times, its self-healing ability also significantly decreased (Figure S20, Supporting Information). PVA enriched phase generated during the freeze-thaw process, which greatly increased the entanglement between molecular chains and reduced the mobility of molecular chains. [9b,15]

Based on the above results, the $PQ_{40}C_5B_{1.5}$ after three times freeze-thaw with optimal mechanical and self-healing properties is selected as the RMSHS. Further loading and unloading experiments (0-150% strain) are conducted in Figure 2f. The large tensile deformation leads to the break of hydrogen bonds and dynamic bonds in the RMSHS network structure, and the reversible intermolecular forces cannot be recovered in time, resulting in a gradual reduction of the maximum stress of the gel. However, it can still maintain more than 81% of the maximum stress and possesses good anti-fatigue performance after 100 cycles. Figure S21 (Supporting Information) shows the hysteresis loop of hydrogel under 40–280% strain, which proves that RMSHS has low hysteresis due to the reversible intermolecular interactions. RMSHS with three times freeze-thaw shows good transparency (Figure 2g; Figure S22, Supporting Information), which also could withstand different deformations such as stretching, knotting, and twisting (Figure 2h). As shown in Figure S23 (Supporting Information), RMSHS possesses a water content of up to 90%. Meanwhile, RMSHS is capable of holding more than 100 times its weight (Figure 2i). The sections of the two stained hydrogels are contacted for 12 h (At room temperature, without wind), and the two parts are bonded into one monolithic hydrogel (Figure 2j). The ε_b and σ_b of RMSHS after self-healing for 3 h at room temperature can reach 96% and 40%, respectively (Figure 2k; Figure S24a,b, Supporting Information). We have observed a significant disparity in the self-healing efficiency between strain and stress within RMSHS. It is because that the self-healing ability of RMSHS is mainly derived from the reconstruction of the "soft" regions consist of hydrogen bonds between N-CQDs and molecular chains and the boronic ester bonds (Figure 2l).

When fractured areas come into contact with each other, the dynamic and "soft" hydrogen bonds and borate ester bonds can reform at room temperature quickly, whereas the "hard"

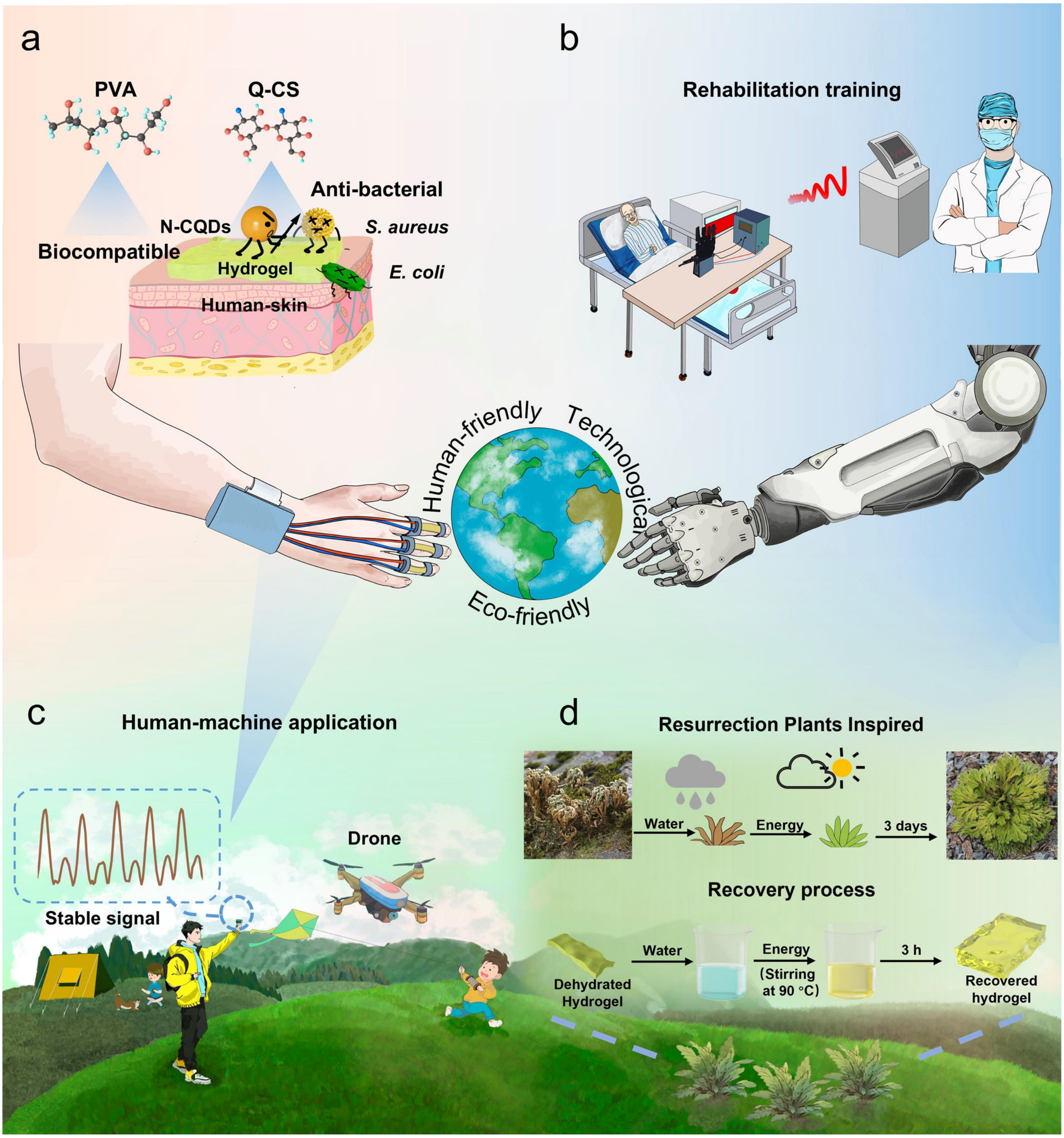

Figure 1. Application of RMSHS in various scenarios. a) Antibacterial properties and biocompatibility of RMSHS. b) RMSHS for medical rehabilitation training. c) Remote real-time control by human hand gestures. d) Simple and efficient green recycling like resurrected plants.

hydrogen bonds within the PVA crystalline microdomains cannot reform without external intervention. Therefore, the self-healed RMSHS still possesses good elongation properties, but due to the absence of PVA crystalline domains serving as crosslinking points to dissipate external forces, the strength of RMSHS is significantly reduced. Furthermore, the cross-linking points formed by these "hard" hydrogen-bonding regions significantly restrict the mobility between molecular chains, further diminishing the likelihood of forming dense hydrogen-bonding regions among molecular chains at the fracture sites. To demonstrate this point, we investigated the self-healing efficiency of RMSHS at different temperatures as shown in Figure S25a–d (Supporting Information). The healed RMSHS at 45 °C can achieve a breaking stress that is 91.9% of its initial state without

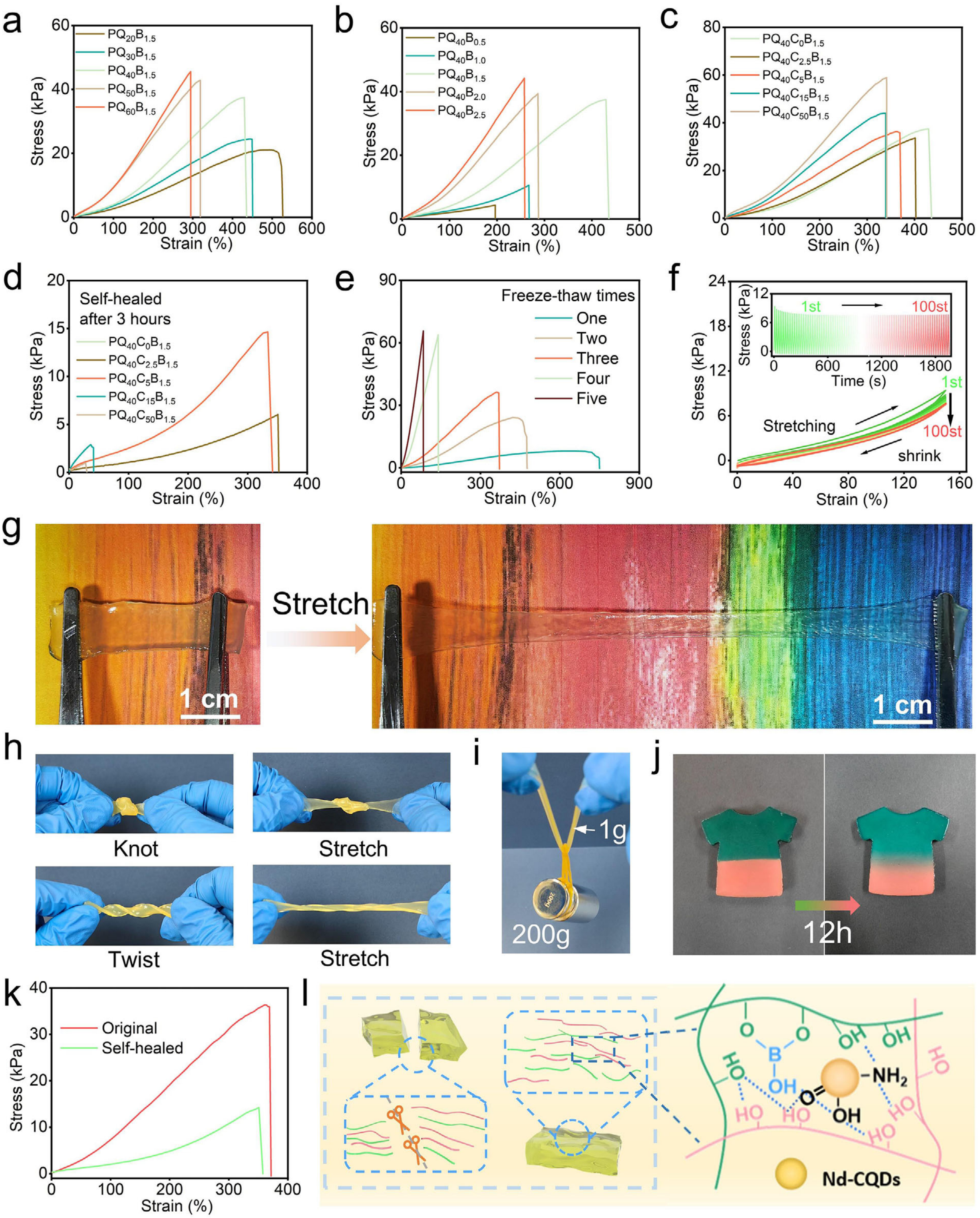

Figure 2. Exploration of optimal content of hydrogel. a,b) Mechanical properties of PQB with different content of QCS and borax. c) Mechanical properties of PQCB with different content of N-CQDs and d) the corresponding self-healing properties of PQCB with different content of N-CQDs. e) Mechanical properties of PQCB with different freeze-thaw times. f) Loading and unloading experiments with constant strain 0–150%. g) Physical picture of RMSHS with three freeze-thaw times. h) Macrograph of RMSHS stretching in different states. i) Lifting and pulling loads. j) Physical image of self-healing hydrogel. k-l) Mechanism of self-healing ability of RMSHS and mechanical properties of initial and self-healed RMSHS.

applying any external force. When the temperature rises to the range of 60–90 °C, the breaking strain of the repaired RMSHS exceeds its initial state, but its fracture stress decreases rapidly. When the temperature is appropriately increased, the chain mobility enhances. However, at excessively high temperatures, some of the partially rigid microdomains within the PVA crystals will be disrupted, leading to the destruction of the polymer network. Based on the above explorations, it is not difficult to predict that further treating the healed RMSHS (90 °C for 3 h) with freezing can enhance its breaking stress and toughness. However, the high temperatures and extreme cold required for these thermally reversible reactions cannot be directly applied to physiological environments and are difficult to control in practical applications. Therefore, we will not delve into this aspect excessively. Instead, we are more inclined to demonstrate its rapid mechanical and electrical self-healing properties at room temperature, which are crucial for ensuring its service life. Figure S26a–d (Supporting Information) illustrates the rapid self-healing capability of RMSHS in a closed circuit. Two pieces of disconnected hydrogel are tightly integrated into the original hydrogel (healed) after 10 s, and the recovered hydrogel could further withstand different degrees of stretching. The hydrogel can be used as a wire to light an LED bulb. RMSHS possesses rapid self-healing ability, excellent durability, and low hysteresis at the same time, which can greatly improve the service life of RMSHS in practical applications.

2.2. Antibacterial Property of RMSHS

RMSHS with biocompatibility and antibacterial properties can be directly adhered to human skin and help patients carry out medical rehabilitation training by constructing a set of intelligent rehabilitation systems. We evaluate the antibacterial property of the RMSHS against Staphylococcus aureus (*S. aureus*) (Gram-positive bacteria) and Escherichia coli (*E. coli*) (Gram-negative bacteria). The number of viable bacteria significantly decreases (**Figure 3a**) and the bactericidal rates of RMSHS against *S. aureus* and *E. coli* are 99.8% and 99.9%, higher than $PQ_{40}B_{1.5}$ and $PC_5B_{1.5}$ (Figure 3b). Additionally, even after 7 days of exposure, the killing rate of all tested microorganisms is still more than 92.3%, implying that RMSHS is effective against *S. aureus* and *E. coli*. The polycationic structure of QCS should have a positive effect on the interaction with the anionic components present on the surface of the microorganisms, boosting antimicrobial activity.[10] Moreover, the bactericidal mechanism of N-CQDs is based on the destructive effect of CQDs on the gene of the bacteria.[11,16] We have demonstrated that nitrogen-doped carbon quantum dots (N-CQDs) possess a large number of amino and imino groups, which are prone to being protonated and thus carrying positive charges. As shown in Figure 3c, the cell wall of *E. coli* is primarily composed of peptidoglycan and lipopolysaccharide. Among them, lipopolysaccharide, located in the outermost layer of the cell wall, is a unique component of Gram-negative bacteria. Lipopolysaccharide molecules contain numerous negatively charged groups, such as carboxyl groups and phosphate groups, which release hydrogen ions when dissociated in water, thereby rendering the surface of *E. coli* negatively charged. [25] *S. aureus* is a Gram-positive bacterium, and its cell wall is primarily composed of peptidoglycan. The peptidoglycan structure contains a large amount of teichoic acid, which is an acidic polysaccharide carrying a negative charge. As shown in Figure S27a–f (Supporting Information), the zeta-potentials of *S. aureus* and *E. coli* are -19.9 mV and – 40.3 mV, confirming the negatively charged property. The zeta potential of the N-CQDs solution with a concentration of 5 mg mL^{-1} is 8.69 mV, demonstrating that the surface of N-CQDs carries a positive charge. With the addition of 5 mg mL^{-1} of N-CQDs, the zeta-potentials of the *S. aureus* and *E. coli* system show a significantly positive shift at 1.52 and 1.10 mV, respectively. These results suggest that *S. aureus* or *E. coli* absorb N-CQDs via electrostatic interactions ascribed to the negatively charged teichoic acids on the membrane surface of *S. aureus* or the thin negatively charged cell membrane of *E. coli*. As shown in Figure S27a,g,h, (Supporting Information), when QCS is mixed with N-CQDs solution and added into *S. aureus* and *E. coli* solutions. The zeta potential values of the *S. aureus* and *E. coli* solutions are 49.1 and 43.7 mV, respectively. The dramatic shift from zeta potential shows that positively charged QCS greatly enhances the electrostatic interactions in the system.

Further, we explore the effects of different concentrations of N-CQDs on the antibacterial efficiency. As shown in Figure S28a,b (Supporting Information), a significantly higher mortality rate of *S. aureus* compared to *E. coli* can be observed at low concentrations of N-CQDs solution (81.5%/ 60.6%, $1{\times}10^{-4}$ g mL^{-1}), (85.3%/ 78.5%, $1{\times}10^{-3}$ g mL^{-1}), which is also reported in previous literature. The cell wall of Gram-positive bacteria is mainly composed of peptidoglycan and phosphatidic acid. The structure is relatively loose but thick. The cell wall of Gram-negative bacteria includes two layers of peptidoglycan and an outer membrane containing lipopolysaccharides. The structure is intensive and thin. Although the N-CQDs could be adsorbed on the bacterial cells via electrostatic interaction, the loose but thick cell membrane structure of Gram-positive bacteria was more appropriate to absorb N-CQDs than that of Gram-negative bacteria with intensive and thin cell wall structure. Therefore, at low concentrations, N-CQDs are more likely to be adsorbed by Gram-positive bacteria, thus showing higher antibacterial efficiency against *S. aureus*.[26] When the concentration of N-CQDs in the culture medium is continuously increased, the antibacterial efficiency against *E. coli* and *S. aureus* is also significantly improved. When the concentration of N-CQDs solution reached 0.1 g mL^{-1}, the mortality rate of both bacteria reaches 99%. However, when serving as a functional filler in PQCB hydrogel, it is imperative to consider not only the antibacterial properties imparted by N-CQDs to the material but also the ramifications of an excessive concentration of N-CQDs on the mechanical properties of PQCB hydrogel. Therefore, we prefer to select an appropriate concentration of N-CQDs in combination with QCS to achieve excellent antibacterial performance.

As a crucial factor in material design, the biocompatibility of RMSHS has also been further evaluated. Benefiting from the selection of PVA and QCS polymer matrices,[27] along with the environmentally friendly physical modulation method of freeze-thawing and the excellent non-toxicity of N-CQDs,[28] RMSHS demonstrates exceptional biocompatibility. As shown in Figure 3d, GES-1 cells are cultured with the leaching solution of RMSHS for a certain period to assess the cytotoxicity of RMSHS. The methyl thiazolyl tetrazolium (MTT) cell proliferation experiment is evaluated quantitatively after 1, 3, and 5 days of culture.

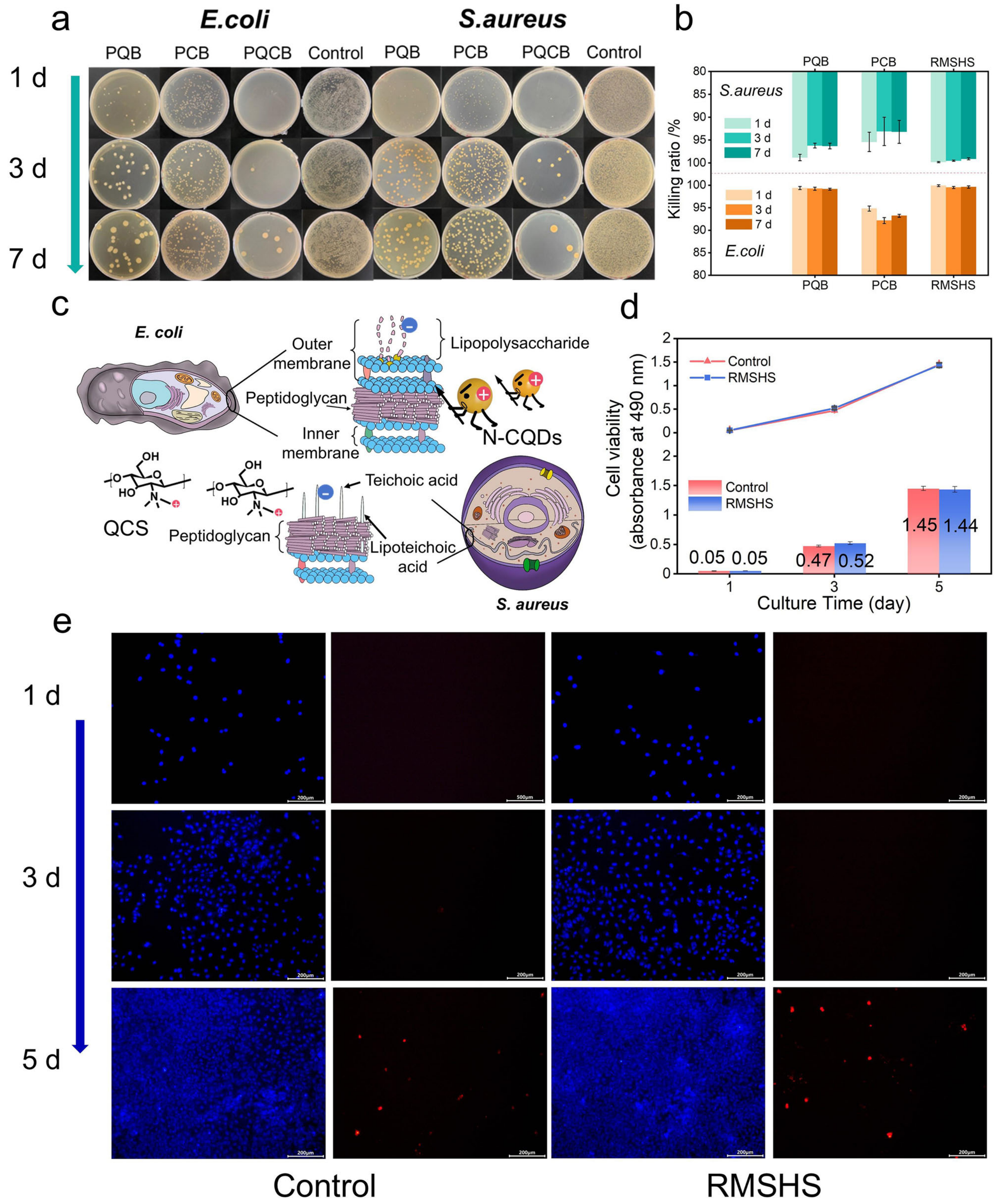

Figure 3. Antibacterial properties and biocompatibility of RMSHS. a) Photograph of *E. coli* and *S. aureus* on the control group (PB), PQB, PCB, and RMSHS(PQCB). b) Antibacterial capacity of PQB, PCB and RMSHS (PQCB) against *E. coli* and *S. aureus*. All the data are shown as the mean ± SD. Error bars, n = 3. c) The mechanism of antimicrobial properties of RMSHS (PQCB). d) Cell viability of GES-1 cultured with the control group (PB) and RMSHS (PQCB). The comparison of optical density of GES-1 cultured with a control group and RMSHS for 1, 3, and 5 days. e) GES-1 cells live staining images of the control group and RMSHS.

Compared with the control group, no significant change in the number of cells is observed in the RMSHS groups, indicating that RMSHS is non-cytotoxic (Figure 3d). The Hoechst 33 342 and Propidium Iodide (PI) staining are employed to visually observe the state of the cells. Figure 3e displays that most of the GES-1 cells in the RMSHS group show a standard fusiform morphology, which exhibits the same proliferation trend as the control group, further demonstrating the good biocompatibility of the RMSHS.

2.3. Recyclability of RMSHS

In large-scale HMI scenarios, the recyclable performance of the medium is crucial to the harmonious development of ecology and technology. The recycling process of RMSHS is simple and suitable for centralized recovery treatment (**Figure** 4ai–iv). When hydrogels are unable to be used due to water loss (Figure S29, Supporting Information; Figure 4a-ii), they can be recycled directly as raw materials by adding the right amount of deionized water (Figure 4a-iii). RMSHS can be processed into different shapes (Figure S30, Supporting Information; Figure 4a-iv), which further facilitate the recycling process of discarded RMSHS sensors. For example, the precursor of the RMSHS can be poured into containers of any shape for transport and storage. The whole “Resurrection process” is similar to the resurrected plants.(Figure 4b-i) More importantly, in the actual operation process, it can be divided into two steps, as shown in Figure 4b-ii, when the hydrogel fails and can no longer be used, it can be centrally recycled: the failed hydrogels are thoroughly dried and then cut into sheets. After weighing, the appropriate amount of deionized water is added, and the precursor of PQCB is obtained by heating and stirring in a water bath. The precursor is poured into customized molds to obtain hydrogels with different shapes repeatedly (Figure 4b-iii). The recycling process produces no waste, which does not require any chemical reagents for purification. There are two main intermolecular interactions in the hydrogel system, reversible hydrogen bonds and dynamic covalent borate lipid bonds. At a certain temperature, the molecular motion breaks the ordered arrangement of hydrogen bonds, and the molecules with functional groups such as hydroxyl return to a certain free molecular state. Therefore, the anhydrous RMSHS can achieve a regeneration effect like “resuscitated plants” under the condition of appropriate temperatures and sufficient water sources.

To explore the change of the intermolecular forces in the hydrogel during the heating process, the variable temperature fourier-transform infrared spectroscopy (VT-FTIR) was carried out from 30 to 150 °C and analyzed using two-dimensional correlation spectroscopy (2D cos). According to the temperature-variable FTIR spectra, the v(O-H) shifts to high wavenumbers with increasing temperature and the peak intensity sharply decreases, indicating that increasing temperature leads the associated hydroxy groups (hydrogen bonding between -OH and -OH groups and hydrogen bonding between -OH and -NH_2) to become free hydroxy.[29] Oppositely, v(B-O-C) undergoes an increase in peak intensity, indicating the increasing temperature also facilitates the formation of borate ester bonds (B-O-C) between boric acid and the disassociated -OH (Figure 4c; Figure S31, Supporting Information). As presented in Figure S32a (Supporting Information), the intensity of typical peak around 1650 cm^{-1} of hydrogen-bonded C═O bonds decreased. The shoulder peak around 1720 cm^{-1}, which represents the free C═O bond, becomes more prominent, indicating that the hydrogen-bonded C═O bonds blue-shifted to 1720 cm^{-1} of free C═O bonds during heating. In this process, the hydroxyl groups are consumed by esterification,[23d] while the number of borate ester bonds is gradually increased. In addition, it is found that the main dissociation temperature of “soft” hydrogen bonds is very close to room temperature, so these dynamic bonds can be rapidly broken and rebuilt under indoor conditions (Figure S32b,c, Supporting Information).

According to the rules of Noda, [30] the 2Dcos are further generated from Figure 4c (Figure 4d). The symbols of the cross peaks of ν_1 and ν_2 are obtained from the results of the 2D synchronous and asynchronous spectral (Tables S1–S3, Supporting Information). When cross-peaks (ν_1, ν_2) in the synchronous and asynchronous maps hold the same symbol, both negative or both positive, then it is inferred that the change at $\nu 1$ takes place prior to that at ν_2 under the perturbation; while if cross-peaks (ν_1, ν_2) in the synchronous and asynchronous spectra hold different symbols, one negative and the other one positive, then it is deduced that the band at ν_2 changes earlier than the band at ν_1. The corresponding response order of the PQBC system to the increasing temperature is 3483 → 3303 → 1327 cm^{-1} (→ presents prior to or earlier than), which means, ν(-NH_2) → ν(-OH) → ν(B-O-C). The results suggest that the -NH_2 groups respond to the disturbance of temperature before the -OH groups further leading to the formation of borate ester bond (Figure 4e). The main disassociation temperatures of hydrogen bonds are very close to room temperature, and these dynamic bonds can quickly break and rebuild under room temperature. [2d] At different temperatures, the amount of hydrogen bonds and borate bonds in RMSHS also change accordingly, indicating that the reversible intermolecular interaction forces in RMSHS could be relatively balanced again by adjusting the external environment.

The freezing time required for the recovered RMSHS is significantly reduced compared to the initial RMSHS. The influence of different freezing durations on the mechanical properties of recovered RMSHS (R-RMSHS) is also explored (Figure S33a–c, Supporting Information). The freezing time of R-RMSHS is greatly reduced and the self-healing performance of R-RMSHS decreases rapidly with the increase of freezing time. The R-RMSHS (freezing for 3 h) possesses a good self-healing ability (Figure S34, Supporting Information). When the freezing time exceeds 9 h, R-RMSHS hydrogel completely loses its self-healing ability. It is supposed that although the solution of recycled RMSHS presents a uniform state under 90 °C, there are still some intramolecular hydrogen bonds and intermolecular hydrogen bonds between the molecular chains; when the hydrogel is cooled at -20 °C again, the polymer chains enrichment regions can be formed fast. As manifested in Figure S35 (Supporting Information), the 100 stretching-releasing cycles under 150 strains are performed on the recycled hydrogel and the hydrogels still have good mechanical properties. In conclusion, the recovery process of RMSHS is simple and the R-RMSHS has excellent properties as the original RMSHS.

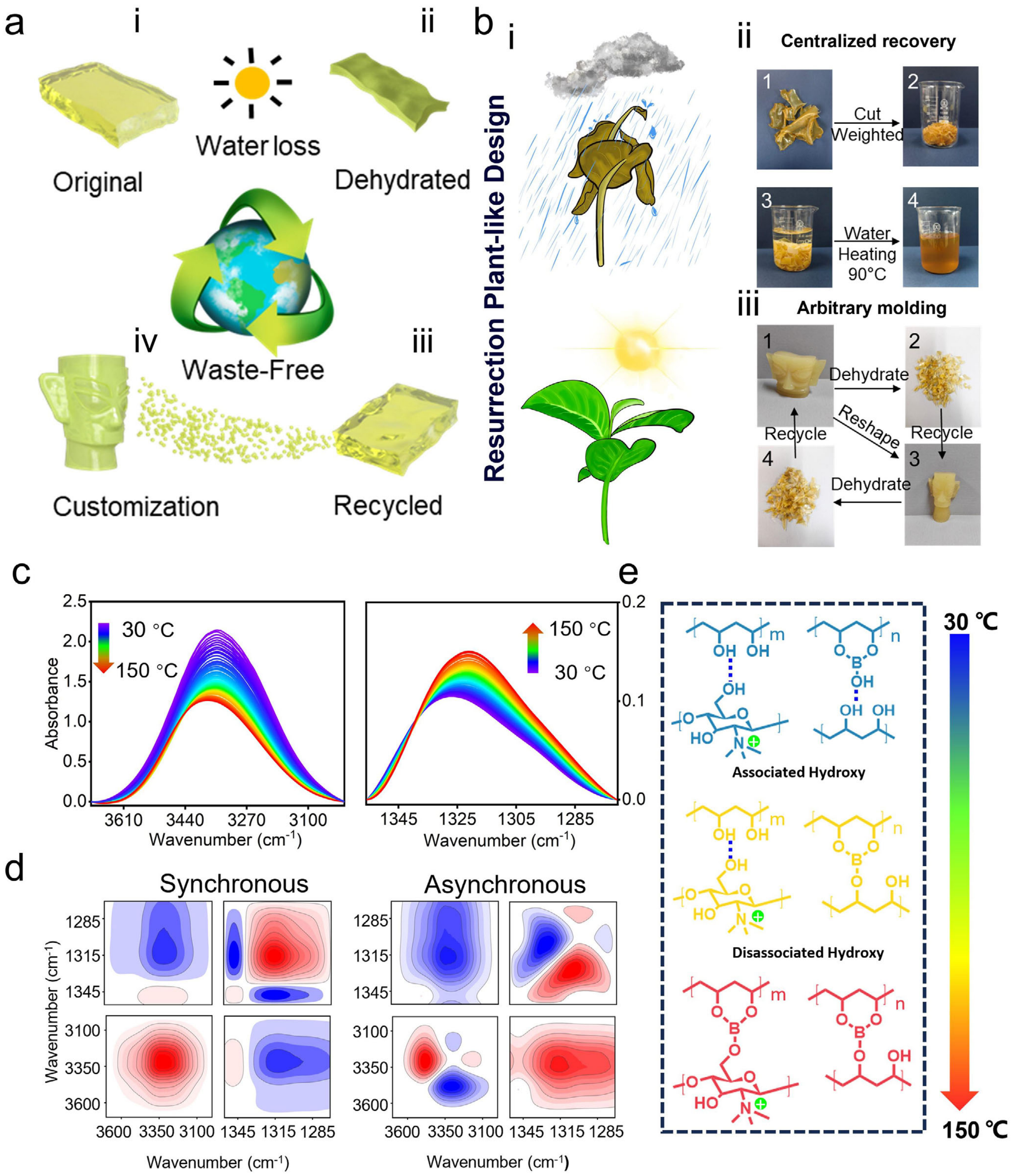

Figure 4. Recyclable properties and the mechanism of the RMSHS. a) Recovery process of RMSHS. b) Physical diagram of the recovery process of RMSHS. c) The temperature variable FTIR spectra of RMSHS (30-150 °C) in the regions of ν(-OH) and ν(B-O-C). d) The 2D synchronous and asynchronous spectra of RMSHS generated from (Figure 4c). e) Schematic diagram of changing intermolecular forces in RMSHS during the heating process.

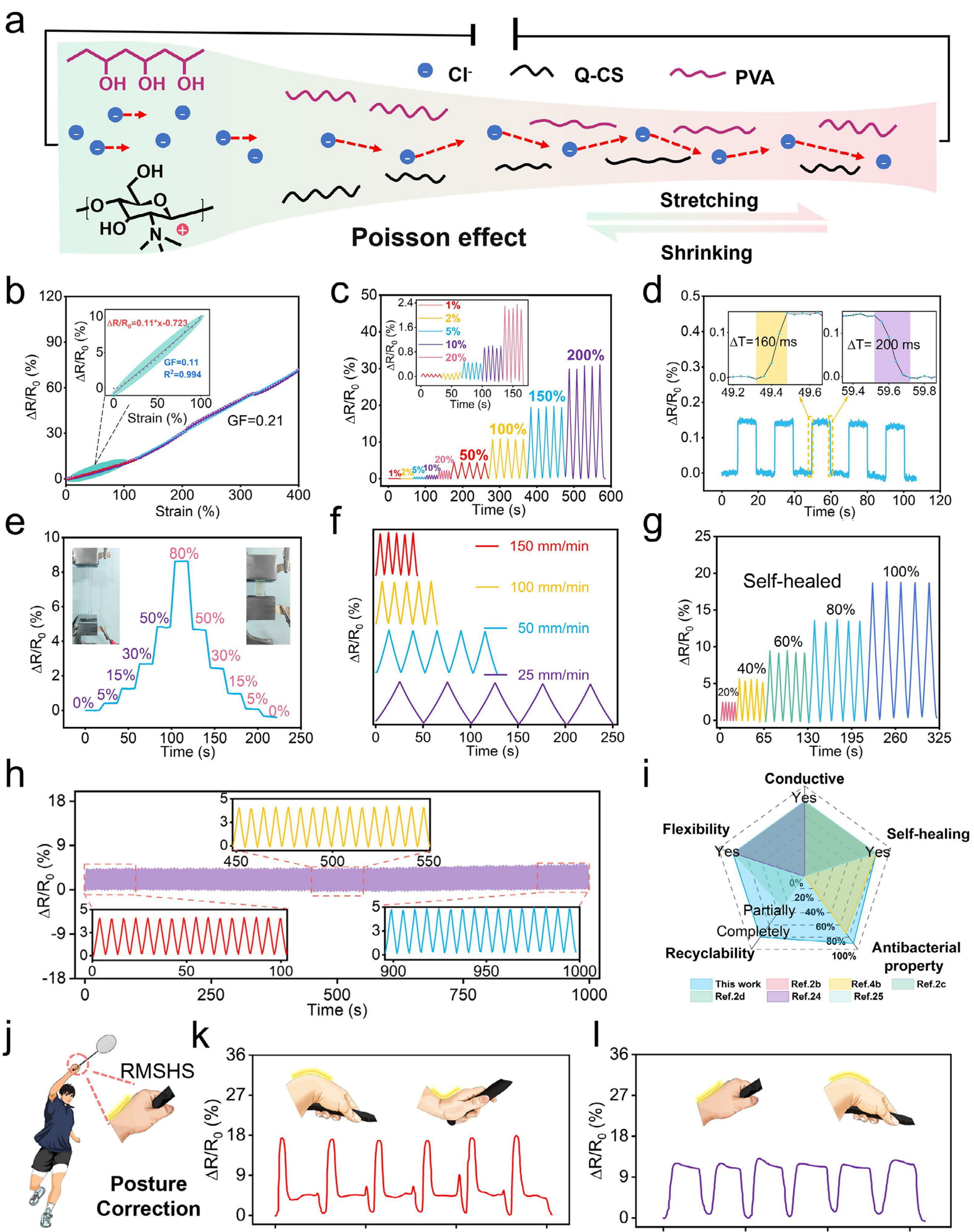
a
OH OH OH
Cl⁻
Q-CS
PVA
OH
O
O
HO
N
Poisson effect
Stretching
Shrinking
b
ΔR/R₀ (%)
Strain (%)
ΔR/R₀=0.11*x-0.723
GF=0.11
R²=0.994
GF=0.21
c
ΔR/R₀ (%)
Time (s)
1%
2%
5%
10%
20%
50%
100%
150%
200%
d
ΔR/R₀ (%)
Time (s)
ΔT=160 ms
ΔT= 200 ms
e
ΔR/R₀ (%)
Time (s)
0%
5%
15%
30%
50%
80%
50%
30%
15%
5%
0%
f
ΔR/R₀ (%)
Time (s)
150 mm/min
100 mm/min
50 mm/min
25 mm/min
g
ΔR/R₀ (%)
Time (s)
Self-healed
20%
40%
60%
80%
100%
h
ΔR/R₀ (%)
Time (s)
i
Conductive
Yes
Self-healing
Yes
Antibacterial property
0%
20%
40%
60%
80%
100%
Recyclability
Completely
Partially
Flexibility
Yes
This work
Ref.2b
Ref.4b
Ref.2c
Ref.2d
Ref.24
Ref.25
j
RMSHS
Posture Correction
k
ΔR/R₀ (%)
Time (s)
l
ΔR/R₀ (%)
Time (s)

2.4. Sensing Properties of RMSHS

RMSHS has extremely stable sensing performance, which is critical performance for HMI medium. As shown in Figure S36a (Supporting Information), special electrodes and fixtures are designed to ensure accuracy and repeatability of the measurements. The silver paste is used to reduce the contact resistance between the conductive hydrogel and the conductive tape. The hydrogel sample's conductivity (σ, S m^{-1}) was calculated using the formula as follow:

$$\sigma = \frac{L}{R \times S} \tag{1}$$

where L represented the distance between the two conductive tapes affixed to hydrogel samples, R represents the measured hydrogel samples resistance, and S indicated the cross-sectional area of the hydrogel samples. The average cross-sectional area of all the PQCB gel samples used for testing was 0.1± 0.006 cm^2, and the distance between the two conductive tapes was an average of 3± 0.2 cm. After calculation, the conductivity of pure PVA hydrogel (hydrogel containing only borax) is 0.025 S m^{-1}, and the addition of N-CQDs (5.0 mg mL^{-1}, the optimal content of PQCB) does not greatly improve the conductivity of hydrogel (0.036 S m^{-1}). The QCS significantly improves the conductivity of the hydrogel, and the final conductivity of the PQCB hydrogel is 0.181 S m^{-1}(Figure S36b, Supporting Information). We also explored the influence of different contents of QCS on the conductivity of PQCB gel. With the increase of QCS content, the conductivity of PQCB hydrogel increased significantly, but the increase in conductivity was no longer obvious after the further increase of QCS content. (Conductivity of $PQ_{50}C_5B_{1.5}$ is 0.192 S m^{-1}) (Figure S36c, Supporting Information) QCS enhances the antibacterial properties of hydrogels and increases the content of free ions in hydrogels, resulting in a 620% increase in electrical conductivity compared to PB hydrogels (Figure S36d, Supporting Information). Due to the Poisson effect, the cross-sectional area of RMSHS gradually decreases during the stretching process; the ion flow channels are squeezed; the conductive ion flow rate decreases, leading to an increase in resistance (**Figure 5**a). The electromechanical properties of RMSHS are characterized by detecting the relative resistance change ($\Delta R/R_0$, $\Delta R = R\text{-}R_0$, R_0 represents the original resistance, R stands for the resistance under strain). The sensitivity is evaluated by GF:[31]

$$GF = \frac{\Delta R/R_0}{\varepsilon} \tag{2}$$

RMSHS has a nearly 400% strain sensing range which can be satisfied with the detection of various human movements (Figure 5b). It's worth mentioning that RMSHS maintains a good linear relationship between output and input within the 100% strain range, which is crucial for long-term monitoring and reliable data recording. RMSHS can accurately detect 1% strain, which possesses the potential to transform small movements of humans into signals. At the same time, the sensing properties of RMSHS from 50% strain to 200% strain are also employed (Figure 5c), indicating that RMSHS possesses good repeatability and sensing discernibility. It is vital to possess fast response/recovery ability (160/200 ms) for realizing real-time controlling and other complex applications (Figure 5d). The stable stepped signal with the stop interval generated by RMSHS (Figure 5e), further demonstrates the stability of RMSHS and its potential for rehabilitation training. Meanwhile, the influence of different stretching speeds on the sensing property of RMSHS could almost be negligible (Figure 5f). The self-healed RMSHS can still possess stable and repeatable sensing performances (Figure 5g). The self-healing features of the RMSHS ensure its stability and durability as strain sensors for practical applications. Furthermore, 150 stretching-releasing cycles under 50% strain are accomplished by RMSHS (Figure 5h), and the sensing stability (Figure S37, Supporting Information) and durability (Figure S38, Supporting Information) of the recycled RMSHS are also demonstrated as the initial RMSHS. Figure 5i shows the functionality of RMSHS compared to the other hydrogel sensors.[2a–c,4b,7a,32] The excellent performances and reusability endow RMSHS with the ability to be used as the ideal medium for large-scale HMI applications, avoiding environmental damage caused by e-waste. RMSHS also has a stable response to human movement, when hitting the ball. The collected signals are analyzed to help athletes correct their posture (Figure 5j). For example, forehand smash (Figure 5k) and retrieve (Figure 5l).

2.5. Applications of RMSHS

An intelligent assisted rehabilitation system is built to mimic the gestures made by the patient and give the patient real-time feedback visually (**Figure 6**a). RMSHS is fixed to the patient's finger, and its low modulus allows it to fit the finger without affecting the flexibility of the finger during training. RMSHS can generate stable electrical signals after 50 cyclic bending deformations (Figure 6b), and the corresponding resistance increment is relative to the bending angle of the finger (Figure S39a,b, Supporting Information). The five channels produce different signals when the patient makes different gestures (Figure 6c), realizing real-time controlling of the robotic hand (Movie S1, Supporting Information).

The patient corrects his finger movements based on the visual feedback from the robotic hand to improve the patient's hand flexibility. In addition, a circuit algorithm is constructed to recognize different gestures made by patients (Figure 6d; Figure S40, Supporting Information). The data can be uploaded to a web page, and doctors can give treatment advice remotely based on their training results (Movie S2, Supporting Information). The operation process of the entire rehabilitation system is shown in Figure 6e, it allows patients to actively engage in rehabilitation

Figure 5. Strain sensing properties of the RMSHS. a) The conduction mechanism of RMSHS. b) Resistance-strain curve. c) The resistance changing curves of the RMSHS after five cycles of tensile recovery at different strains. d) Response and recovery time. e) The step-up and recovery response curves of the RMSHS at different strain ranges. f) Relative resistance changes at different stretching-releasing rates. g) The resistance strain curves of the self-healed RMSHS. h) The 150 multi-cycle response curves of the RMSHS at 50% strain. i) Comparison to previous research. j) Sports monitoring during badminton playing such as k) forehand smash and l) retrieve.

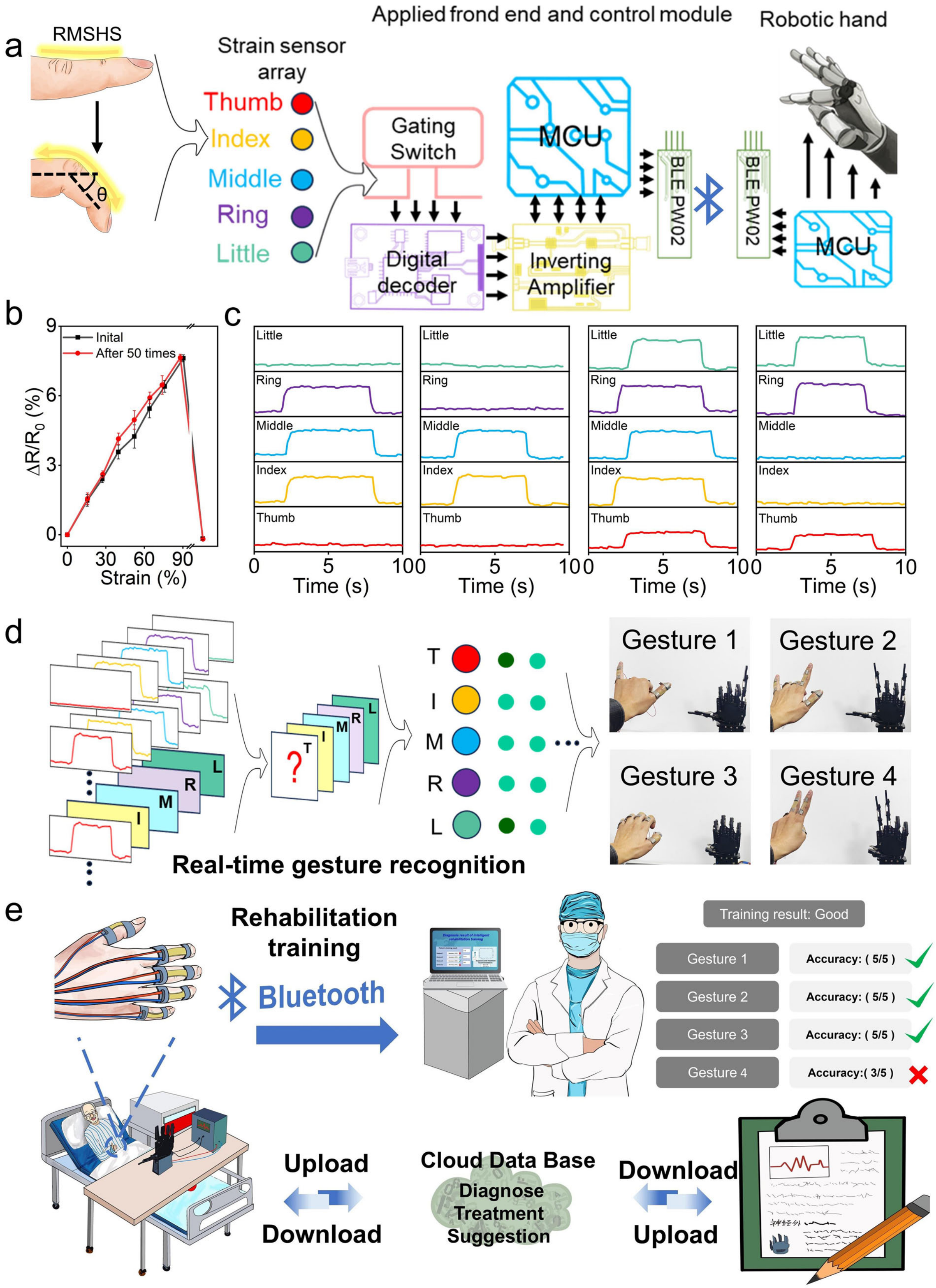
a
RMSHS
θ
Strain sensor array
Thumb
Index
Middle
Ring
Little
Applied frond end and control module
Gating Switch
Digital decoder
MCU
Inverting Amplifier
BLE PW02
BLE PW02
MCU
Robotic hand
b
ΔR/R0 (%)
Inital
After 50 times
0
3
6
9
0
30
60
90
Strain (%)
c
Little
Ring
Middle
Index
Thumb
0
5
10
Time (s)
d
T
I
M
R
L
?
Gesture 1
Gesture 2
Gesture 3
Gesture 4
Real-time gesture recognition
e
Rehabilitation training
Bluetooth
Training result: Good
Gesture 1
Accuracy: (5/5)
Gesture 2
Accuracy: (5/5)
Gesture 3
Accuracy: (5/5)
Gesture 4
Accuracy:(3/5)
Upload
Download
Cloud Data Base
Diagnose
Treatment
Suggestion
Download
Upload

training through feedback from the machine, without the companionship of medical staff. At the same time, doctors can also make remote diagnoses and provide rehabilitation treatment suggestions for patients through the intelligent rehabilitation system, which greatly reduces the burden of medical staff and saves medical resources. The partial code for the above functionality is provided in Figures S41 and S42 (Supporting Information).

Thanks to the excellent stability, biocompatibility, and unique skin-conformability of RMSHS, we further explored its potential applications in more complex HMI scenarios. Accordingly, the control of a UAV systems by RMSHS has been achieved through the integration of RMSHS with Python programming and an intelligent gesture control system developed by the author. RMSHS captures a person's hand movements and transmits the data to an electronic output signal to steer the drone. **Figure 7a** shows the main modules when the intelligent gesture control system is employed in controlling UAV. The whole system consists of three main parts (Figure S43, Supporting Information), 1) RMSHS is attached to human fingers to recognize the finger joint movements (Movie S3, Supporting Information). 2) Signal acquisition, processing, and instruction generation module (Movie S4, Supporting Information). 3)The drive control module is used to control the movement of the UAV in space. When the RMSHS generates the resistance change, the signal is picked up by a signal processing device on the wrist and sent wirelessly to a machine, where it is programmed into different signals. These signals will be parsed by the Python program to generate instructions, which will be sent to the flight control module of the drone through wireless transmission technology, driving the motor to drive the drone in the designable mode.

It is worth noting that this wearable UAV control system can realize three-degree-of-freedom (3-DoF) movement control through only three channels. The channel 1 on the index finger is set with two thresholds corresponding to the change in resistance when the finger is bent by 45 and 90°. When the index finger is bent at different angles, the drone rotates clockwise or counterclockwise in the plane, respectively (Figure 7b). Considering the ease of finger manipulation, the other two channels are placed on the middle finger and ring finger respectively, and both channels set two thresholds to control the up and down movement of the drone and the left and right movement respectively (Figure 7c). Ultimately, 3-DoF flight of the UAV is successfully achieved by RMSHS, as depicted in Movie S5 (Supporting Information). If necessary, python program or circuit signal algorithm processing can be designed to arrange and combine electrical signals in different channels, up to 234 instructions can be reached (5 channels). Considering the flexibility of fingers and the complexity of instructions, this work does not demonstrate too many instructions but also demonstrates the potential of intelligent gesture systems based on RMSHS in HMI and remote controlling. As a multi-functional HMI medium, RMSHS can be recycled completely and centrally, it can be easily applied to other real-time remote-control platforms like smart cars and other devices to construct the smart city system in the future (Figure 7d). Moreover, RMSHS exhibits outstanding HMI capabilities while being uniquely human-friendly and environmentally friendly, is the ideal next-generation medium of large-scale HMI.

Triboelectric nanogenerator (TENG), environmentally friendly energy-harvesting devices based on the combination of contact electrification and electrostatic induction.[33] In the structure of TENG, the traditional metal electrodes exhibit poor environmental friendliness, as the disposal of metal waste is difficult to degrade and thereby increases environmental burden. Furthermore, for wearable devices, the rigidity of these metal electrodes mismatches with the flexibility of the substrate materials, resulting in a decline in performance. As illustrated in **Figure 8a**, RMSHS possesses the ideal characteristics of being environmentally friendly and recyclable, self-healing, biocompatible, flexible, as well as stretchable, making it an exemplary green electrode material in TENG. Therefore, a sandwich-structured RMSHS-based TENG (R-TENG) is constructed, including the PU film as the contact triboelectric material layer and the RMSHS as the electrode layer. Figure S44 (Supporting Information) displays the working mechanism of the RMSHS in single electrode TENG mode. i) When the Polydimethylsiloxane (PDMS) layer contacts the PU film under external pressure, due to the difference of electronegativity between the PDMS layer and the PU layer, positive charges are generated at the PU layer while the PDMS layer carries the negative charges. ii) When the PDMS layer is removed, due to electrostatic induction, the positive charges on the PU film induce the free electrons to accumulate on the surface of the recyclable hydrogel electrode layer while free electrons move from the ground towards the recyclable hydrogel layer. iii) When the distance between the PDMS layer and the PU layer is the largest, the negative charges on the PDMS and the positive charges on the PU film reach a balance iv) When the PDMS layer approaches back to the PU film, the electrons would be repelled back from the recyclable hydrogel electrode to the ground. Alternating current signals can be generated by continuous contact separation between the PDMS layer and the PU layer.

As shown in Figure S45 (Supporting Information), R-TENG displays considerable flexibility and deformability under different complicated deformations. To further demonstrate the excellent electrical output capability of R-TENG after storage under extreme deformation conditions, voltage under different stretching states is tested. (Figure 8b) The R-TENG is stretched along the uniaxial direction with different stretching ratios while the area of the impacting force (the size of the PDMS layer, 20 mm × 20 mm) is maintained unchangeably. The voltage decreases with the increasing elongation, while the highly stable output signal could still be produced even under 250% strain, due to that the PU film became thinner along the width direction according to Poisson's effect, leading to the reduction of the effective triboelectric area. Interestingly, the output signal almost returned to the original value after removing the tensile force, displaying that the R-TENG device possesses excellent stability and durability.

Figure 6. The principle of intelligent rehabilitation system and practical application scenario. a) Schematic diagram of visual response module of intelligent rehabilitation system. b) Resistance stability of RMSHS after 50 bending. All the data are shown as the mean ± SD. Error bars, n = 3. c) Resistive response of five channels with different gestures. d) The real-time gesture recognition module diagram of an intelligent rehabilitation system. e) The practical application flow of intelligent active rehabilitation robot system.

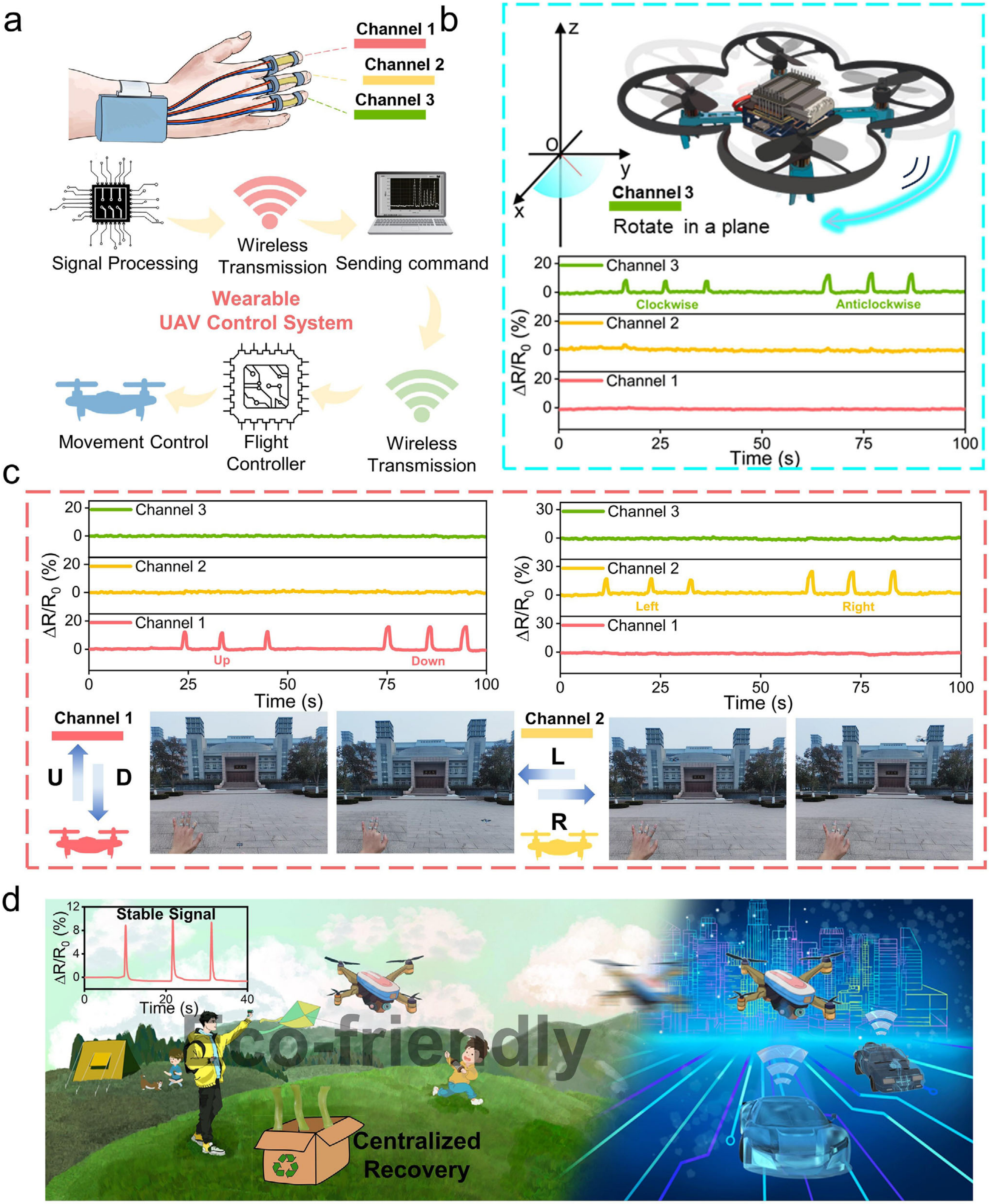

Figure 7. The intelligent real-time remote control system based on RMSHS is applied to 3-DoF UAV control. a) The schematic diagram describes the various modules of the intelligent gesture control system employed in the UAV. b) Control of the rotation angle of the drone in the horizontal plane. c) Schematic diagrams of the RMSHS attached to the hand when acting as a drone flight controller, and the command signals that control the movement of the drone in the vertical plane. d) RMSHS, as a green medium for HMI, has the potential to build future smart cities.

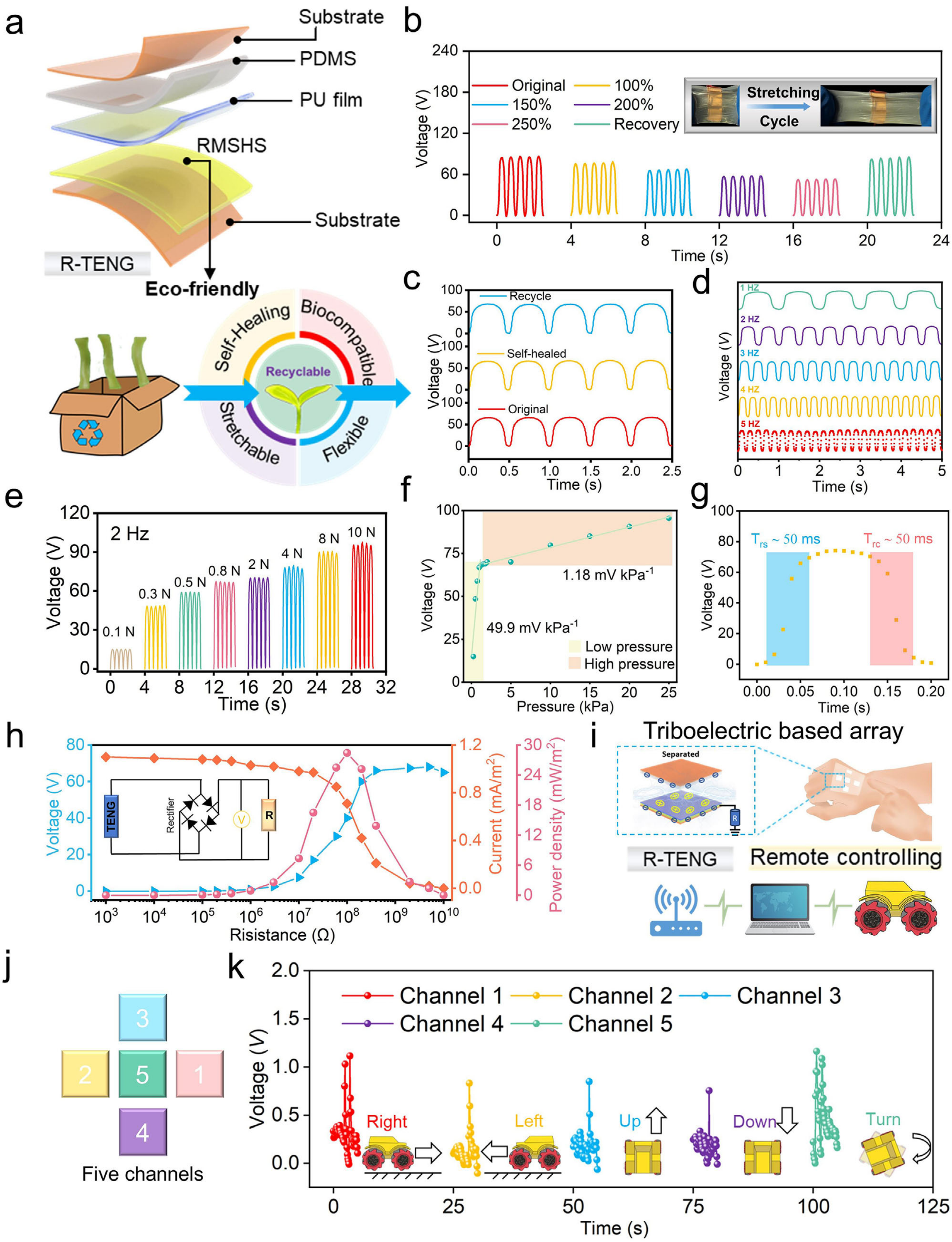
a
Substrate
PDMS
PU film
RMSHS
Substrate
R-TENG
Eco-friendly
Self-Healing
Biocompatible
Recyclable
Stretchable
Flexible
b
Voltage (V)
Time (s)
Original
100%
150%
200%
250%
Recovery
Stretching
Cycle
c
Voltage (V)
Time (s)
Recycle
Self-healed
Original
d
Voltage (V)
Time (s)
1 HZ
2 HZ
3 HZ
4 HZ
5 HZ
e
Voltage (V)
Time (s)
2 Hz
0.1 N
0.3 N
0.5 N
0.8 N
2 N
4 N
8 N
10 N
f
Voltage (V)
Pressure (kPa)
1.18 mV kPa^{-1}
49.9 mV kPa^{-1}
Low pressure
High pressure
g
Voltage (V)
Time (s)
T_{rs} ~ 50 ms
T_{rc} ~ 50 ms
h
Voltage (V)
Current (mA/m^2)
Power density (mW/m^2)
Risistance (Ω)
TENG
Rectifier
V
R
i
Triboelectric based array
Separated
R
R-TENG
Remote controlling
j
3
2
5
1
4
Five channels
k
Voltage (V)
Time (s)
Channel 1
Channel 2
Channel 3
Channel 4
Channel 5
Right
Left
Up
Down
Turn

Due to its good self-healing ability, the self-healed RMSHS can still produce electrical signals as stable as the initial and recovered RMSHS (Figure 8c; Figure S46, Supporting Information). It helps alleviate issues related to frictional wear and stress concentration through self-healing. Moreover, the voltage of the R-TENG is almost the same when the frequency is applied in the range of 1–5 Hz at a pressure of 1 N (Figure 8d), demonstrating the excellent sustainability of RMSHS as an electrode. The voltage of the R-TENG increases from 15 to 68 V with an increasing force (0.1-0.8 N) and the voltage increases from 70 to 95 V with augmenting pressure from 2 to 10 N, which can distinguish different pressure, indicating huge potential application prospects (Figure 8e). The sensitivity of R-TENG is further discussed through the graphs of the voltage against different pressures (Figure 8f). As expressed in Figure 8g, the response time and the recovery time are 50 and 50 ms, respectively, which can well meet the requirements of dynamic tactile sensing. To gain deeper insights into the energy-harvesting capabilities of the R-TENG within an external circuit configuration, measurements were conducted for output voltage, current density, and instantaneous power density across a spectrum of external load resistances ranging from 1 kΩ to 10 GΩ (depicted in Figure 8h). Adhering to Ohm's law, an inverse relationship was observed: as the load resistance increased, the output voltage of the R-TENG escalated, whereas the current diminished accordingly. Notably, the peak output power density attained its maximum value of 28.4 mW m^{-2} at a load resistance of 100 MΩ. Furthermore, the R-TENG demonstrated remarkable reliability, maintaining stable electrical outputs throughout more than 3000 cycles of contact/separation motion at a frequency of 2 Hz (Figure S47, Supporting Information).

These results affirm R-TENG's robustness and fulfillment of reliability standards essential for practical nanogenerator applications. The R-TENG-based array consists of five 20mm×20 mm R-TENG devices. Thanks to the flexibility, adaptability, and biocompatibility of R-TENGs, they can be easily integrated onto the back of a human hand. By pressing with fingers, mechanical energy is converted into electrical energy, enabling a unique green human-machine interaction (Figure 8i). As shown in Figure 8J,K, Channels 1–5 correspond to the cart's movements to the right, to the left, upwards, downwards, and turning, respectively (Movie S6, Supporting Information). The use of recyclable hydrogel materials as the electrode of the TENG structure, instead of traditional electrode materials, provides a new possibility for the development of green energy.

3. Conclusion

In summary, the ideal medium for HMI with 100% retrievability, rapid self-healing ability, stable strain sensing, biocompatibility, and antibacterial properties is designed by introducing reversible intermolecular interactions, dynamic covalent bonds, and physical crosslinking regulations. The anhydrous RMSHS can achieve a regeneration effect like "resuscitated plants". Additionally, the dynamic transition process of intermolecular interactions during the recycling of RMSHS is successfully observed through in-situ Fourier Transform Infrared (FTIR) spectroscopy, and the sequence of this transition process is further explored using 2D correlation spectroscopy. During the heating process, molecular motion breaks the ordered arrangement of hydrogen bonds, the states of functional groups on molecules like hydroxyl and amine groups change, hydrogen bond breaks, hydroxyl group is consumed by esterification while the borate ester bond is gradually increased. Further, the equilibrium state of the hydrogen bond and borate lipid bond is achieved through the reversible physical crosslinking regulation method of freeze-thaw. In gel-based sensors, this dynamic transition of intermolecular forces during the recycling process has been recorded and analyzed in detail for the first time as we known. Moreover, an autonomous rehabilitation training strategy is proposed, patients can autonomously conduct rehabilitation gesture training according to the real-time feedback of the robot hand. The accuracy of a patient's different gestures can be recognized by the intelligent gesture recognition system and the results of rehabilitation training can be uploaded to the cloud, enabling doctors to provide treatment recommendations to patients remotely. The active rehabilitation system succeeded in lightening the burden on medical staff and improving the efficiency of doctor's diagnoses. The feasibility of the sustainable HMI system in real-time remote controlling UAV is demonstrated. Moreover, the python program or circuit signal algorithm program can also be designed to process signals of different channels according to different usage scenarios. Benefiting from this customizability, the sustainable HMI medium RMSHS could be further employed to other remote sensing platforms to realize real-time controlling, such as robots, intelligent cars, etc. The R-TENG intelligent array, designed based on RMSHS, replaces the electrode consumables in traditional TENGs, achieving a unique human-machine interaction. Simultaneously, it realizes the generation of green energy and 100% recyclability of electrode materials. RMSHS provides possibilities for smart cities and large-scale human-machine interaction scenarios. It primarily solves the problem that hydrogel is easy to become e-waste due to water loss or fracture, and reduces the harm caused by e-waste to the environment, realizing the harmonious development of technology, mankind, and nature.

4. Experimental Section

Fabrication of N-CQDs: Using citric acid as the carbon source and glutathione as the nitrogen source, N-CQDs were synthesized via a segmented melting method, with polyethylene polyamine regulating their size and dispersibility.

Figure 8. A new generation of 100% green and sustainable TENG structures assembled by RMSHS in the field of human-machine interaction. a) A sandwich-structured RMSHS based TENG with self-healing, biocompatibility, stretchability, flexibility and recyclability b) Voltage of R-TENG under different stretching states. c) Voltage of initial, self-healed and recycled RMSHS under the pressure of 1N. d) Frequency-dependent responses of R-TENG under the pressure of 1N. e) Voltage of R-TENG at different pressures (2 Hz). f) The relationship between VOC and pressures. All the data are shown as the mean ± SD. Error bars, n = 3. g) The response time and recovery time of R-TENG. h) Measured output voltage, output current, and output power density with variable load resistances. i) Wearable array based on R-TENG. j-k) Display of functions corresponding to the 1–5 channels of the wearable array.

Fabrication of RMSHS: RMSHS was fabricated using a facile physical cross-linking regulation strategy. The synthesized functional nano-filler N-CQDs were dissolved in the aqueous solution and mixed with PVA and QCS in the designed amounts. The mixed solution was heated in a water bath at 90 °C for 30 min to form a uniform and stable precursor solution. A very small amount of borax was added to the precursor solution and stirred thoroughly to obtain a preliminary cross-linking network-like structure. The 3D cross-network structure is further developed through the physical cross-linking method freeze-thaw cycling.

Characterizations: The morphology of N-CQDs was measured through a transmission electron microscope (TEM, TF20, JEOL-2100F). SEM images were carried out on a microscope (FE-SEM, Zeiss MERLIN Compact). X-ray photoelectron spectroscopy (XPS) was used for the analysis. (Thermo ESCALAB 250XI). Fourier Transform Infrared spectroscopy (FTIR) analysis was carried out using a spectrometer (Thermo Scientific Nicolet iS50). Variable Temperature Fourier-Transform Infrared spectroscopy (VT-FTIR) was carried out using a Nicolet IS50 spectrometer and analyzed using 2D Correlation Spectroscopy Analysis software.

The detailed experimental section can be found in the Supporting Information.

Supporting Information

Supporting Information is available from the Wiley Online Library or from the author.

Acknowledgements

The authors acknowledge the financial support of this research by the National Natural Science Foundation of China (52173048, 52303114, 52125205, 52250398, and 52203307), China Postdoctoral Science Foundation (2023M733199, 2024T170838).

Conflict of Interest

The authors declare no conflict of interest.

Data Availability Statement

The data that support the findings of this study are available from the corresponding author upon reasonable request.

Keywords

biocompatible, human-machine interaction, hydrogel, recyclable, remote real-time controlling, self-healing, strain sensors

Received: April 15, 2025
Revised: May 8, 2025
Published online:

---

[1] a) J. Wang, B. Wu, P. Wei, S. Sun, P. Wu, *Nat. Commun.* **2022**, *13*, 4411; b) Y. Liu, K. He, G. Chen, W. R. Leow, X. Chen, *Chem. Rev.* **2017**, *117*, 12893; c) C. Kaspar, B. J. Ravoo, W. G. van der Wiel, S. V. Wegner, W. H. P. Pernice, *Nature* **2021**, *594*, 345; d) W. Wang, H. Zhou, Z. Xu, Z. Li, L. Zhang, P. Wan, *Adv. Mater.* **2024**, *36*, 202401035; e) H. Wang, Q. Ding, Y. Luo, Z. Wu, J. Yu, H. Chen, Y. Zhou, H. Zhang, K. Tao, X. Chen, J. Fu, J. Wu, *Adv. Mater.* **2024**, *36*, 202309868.

[2] a) C. Zhang, Y. Zhou, H. Han, H. Zheng, W. Xu, Z. Wang, *ACS Nano* **2021**, *15*, 1785; b) H. Wang, Y. Yin, Z. Su, C. Chen, L. Zhang, C. Wang, W. Yang, Y. Huang, P. Xu, P. Ma, T. Liu, P. Ma, *Adv. Funct. Mater.* **2024**, *34*, 2311649; c) Y. Li, Z. Tian, X. Z. Gao, H. Y. Zhao, X. Li, Z. L. Wang, Z. Z. Yu, D. Yang, *Adv. Funct. Mater.* **2023**, *33*, 2308845; d) C. Li, J. Liu, X. Qiu, X. Yang, X. Huang, X. Zhang, *Angew. Chem., Int. Ed.* **2023**, *62*, 202313971.

[3] a) L. Xu, Y. Qiao, D. Qiu, *Adv. Mater.* **2023**, *35*, 2209913; b) Q. Zhang, H. Lu, G. Yun, L. Gong, Z. Chen, S. Jin, H. Du, Z. Jiang, W. Li, *Adv. Funct. Mater.* **2023**, *34*, 2308113.

[4] a) F. Cui, J. Sun, J. Ji, X. Yang, K. Wei, H. Xu, Q. Gu, Y. Zhang, X. Sun, *J. Hazard. Mater.* **2021**, *406*, 124330; b) M. Li, Y. Zhang, L. Lian, K. Liu, M. Lu, Y. Chen, L. Zhang, X. Zhang, P. Wan, *Adv. Funct. Mater.* **2022**, *32*, 2208141.

[5] a) M. Yao, Y. Chen, J. Zhang, F. Gao, S. Ma, F. Guan, *Mater. Today Chem* **2019**, *14*, 100192; b) Y. Gao, S. Gu, F. Jia, G. Gao, *J. Mater. Chem. A* **2020**, *8*, 24175.

[6] a) R. Liu, Y. Liu, Y. Cheng, H. Liu, S. Fu, K. Jin, D. Li, Z. Fu, Y. Han, Y. Wang, Y. Tian, *Adv. Funct. Mater.* **2023**, *33*, 2308175; b) N. Li, Q. Yu, S. Duan, Y. Du, X. Shi, X. Li, T. Jiao, Z. Qin, X. He, *Adv. Funct. Mater.* **2024**, *34*, 2309500.

[7] a) Z. Shen, Z. Zhang, N. Zhang, J. Li, P. Zhou, F. Hu, Y. Rong, B. Lu, G. Gu, *Adv. Mater.* **2022**, *34*, 2203650; b) J. P. Zhang, Y. Hu, L. A. Zhang, J. P. Zhou, A. Lu, *Nano-Micro Lett.* **2023**, *15*, 2311; c) H. Heidari, *Nat. Electron.* **2018**, *1*, 578; d) S. L. Zhang, Y. H. Zhou, A. Libanori, Y. B. Deng, M. Y. Liu, M. J. Zhou, H. Qu, X. Zhao, P. Zheng, Y. L. Zhu, J. Chen, S. C. Tan, *Nat. Electron.* **2023**, *6*, 338.

[8] a) M. Baumgartner, F. Hartmann, M. Drack, D. Preninger, D. Wirthl, R. Gerstmayr, L. Lehner, G. Mao, R. Pruckner, S. Demchyshyn, L. Reiter, M. Strobel, T. Stockinger, D. Schiller, S. Kimeswenger, F. Greibich, G. Buchberger, E. Bradt, S. Hild, S. Bauer, M. Kaltenbrunner, *Nat. Mater.* **2020**, *19*, 1102; b) H. Liu, H. Chu, H. Yuan, D. Li, W. Deng, Z. Fu, R. Liu, Y. Liu, Y. Han, Y. Wang, Y. Zhao, X. Cui, Y. Tian, *Nano-Micro Lett.* **2024**, *16*, 69.

[9] a) M. Gao, J. Mao, *Front. Neurosci.* **2021**, *15*, 780147; b) H. Liu, C. Du, L. Liao, H. Zhang, H. Zhou, W. Zhou, T. Ren, Z. Sun, Y. Lu, Z. Nie, F. Xu, J. Zhu, W. Huang, *Nat. Commun.* **2022**, *13*, 3420; c) M. Costandi, *Nature* **2014**, *510*, S8.

[10] a) J. Li, Q. Ding, H. Wang, Z. Wu, X. Gui, C. Li, N. Hu, K. Tao, J. Wu, *Nano-Micro Lett.* **2023**, *15*, 105; b) Y. Yu, H. Yuk, G. A. Parada, Y. Wu, X. Liu, C. S. Nabzdyk, K. Youcef-Toumi, J. Zang, X. Zhao, *Adv. Mater.* **2019**, *31*, 1807101.

[11] a) Q. Ding, H. Wang, Z. Zhou, Z. Wu, K. Tao, X. Gui, C. Liu, W. Shi, J. Wu, *SmartMat* **2023**, *4*, 1147. b) Y. He, Q. Li, P. Chen, Q. Duan, J. Zhan, X. Cai, L. Wang, H. Hou, X. Qiu, *Nat. Commun.* **2022**, *13*, 7666; c) Z. Wu, H. Wang, Q. Ding, K. Tao, W. Shi, C. Liu, J. Chen, J. Wu, *Adv. Funct. Mater.* **2023**, *33*, 2300046.

[12] a) Y. Guo, K. Zheng, P. Wan, *Small* **2018**, *14*, 1704497; b) D. P. Dubal, N. R. Chodankar, D. H. Kim, P. Gomez-Romero, *Chem. Soc. Rev.* **2018**, *47*, 2065.

[13] a) N. Ben Halima, *RSC Adv.* **2016**, *6*, 39823; b) K. Chen, K. Liang, H. Liu, R. Liu, Y. Liu, S. Zeng, Y. Tian, *Nano-Micro Lett.* **2023**, *15*, 102.

[14] a) B. I. Andreica, X. Cheng, L. Marin, *Eur. Polym. J.* **2022**, *164*, 110963; b) K. Zheng, Y. Tong, S. Zhang, R. He, L. Xiao, Z. Iqbal, Y. Zhang, J. Gao, L. Zhang, L. Jiang, Y. Li, *Adv. Funct. Mater.* **2021**, *31*, 2102599.

[15] a) Y. Wang, T. Lv, K. Yin, N. Feng, X. Sun, J. Zhou, H. Li, *Small* **2023**, *19*, 2207048. b) Z. Li, J. Lu, T. Ji, Y. Xue, L. Zhao, K. Zhao, B. Jia, B. Wang, J. Wang, S. Zhang, Z. Jiang, *Adv. Mater.* **2024**, *36*, 2306350. c) J. Yang, V. Cristian, A. Dong, J. Zhang, *Macromol. Chem. Phys.* **2021**, *222*, 2000429.

[16] a) Y. Gong, Y. Hu, Y. Cheng, Z. Liu, Y. Gu, X. Yin, H. Ding, H. Yang, M. Kang, Y. Wei, D. Huang, *J. Mater. Sci.* **2022**, *57*, 12947; b) G. Nian, J. Kim, X. Bao, Z. Suo, *Adv. Mater.* **2022**, *34*, 2206577.

[17] a) Z. Guo, X. Lu, X. Wang, X. Li, J. Li, J. Sun, *Adv. Mater.* **2023**, *35*, 2300286; b) X. Hu, M. Vatankhah-Varnoosfaderani, J. Zhou, Q. Li, S. S. Sheiko, *Adv. Mater.* **2015**, *27*, 6899.

[18] a) J. C. Lai, J. F. Mei, X. Y. Jia, C. H. Li, X. Z. You, Z. Bao, *Adv. Mater.* **2016**, *28*, 8277; b) Y. Shao, G. Du, B. Luo, T. Liu, J. Zhao, S. Zhang, J. Wang, M. Chi, C. Cai, Y. Liu, X. Meng, Z. Liu, S. Wang, S. Nie, *Adv. Mater.* **2024**, *36*, 2311993.

[19] a) H. Takeno, H. Inoguchi, W.-C. Hsieh, *Cellulose* **2020**, *27*, 4373; b) J. L. Holloway, A. M. Lowman, G. R. Palmese, *Soft Matter* **2013**, *9*, 826.

[20] X. Hao, L. Huang, C. Zhao, S. Chen, W. Lin, Y. Lin, L. Zhang, A. a. Sun, C. Miao, X. Lin, M. Chen, S. Weng, *Mater. Sci. Eng. C.* **2021**, *123*, 111971.

[21] a) J. Zhang, Y. Yuan, M. Gao, Z. Han, C. Chu, Y. Li, P. C. M. van Zijl, M. Ying, J. W. M. Bulte, G. Liu, *Angew. Chem., Int. Ed.* **2019**, *58*, 9871; b) S. Zhu, Q. Meng, L. Wang, J. Zhang, Y. Song, H. Jin, K. Zhang, H. Sun, H. Wang, B. Yang, *Angew. Chem. In. Ed.* **2013**, *52*, 3953.

[22] Y. J. Chung, K. Kim, B. I. Lee, C. B. Park, *Small* **2017**, *13*, 1700983.

[23] a) J. Li, Z. Zhang, X. Cao, Y. Liu, Q. Chen, *Soft Matter* **2018**, *14*, 6767; b) A. Dixit, D. S. Bag, S. J. S. Kaira, *Polymer* **2017**, *119*, 263; c) N. Shawgi, S. Li, S. Wang, *Ceram. Int.* **2017**, *43*, 10554; d) I. Yanase, R. Ogawara, H. Kobayashi, *Mater. Lett.* **2009**, *63*, 91; e) Y. Yue, J. Gu, J. Han, Q. Wu, J. Jiang, *J. Hazard. Mater.* **2021**, *401*, 123798.

[24] a) F. Liu, X. Zhang, X. Xiao, Q. Duan, H. Bai, Y. Cao, Y. Zhang, M. Alee, L. Yu, *Carbohyd. Polym* **2023**, *312*, 120755; b) Z. Wang, F. Cheng, H. Cai, X. Li, J. Sun, Y. Wu, N. Wang, Y. Zhu, *Carbohyd. Polym* **2021**, *259*, 117753.

[25] a) C. L. Zhu, Q. Yang, L. B. Liu, S. Wang, *J. Mater. Chem. C* **2011**, *21*, 7905; b) A. Pal, S. O. Pehkonen, L. E. Yu, M. B. Ray, *J. Photochem. Photobio. A.* **2007**, *186*, 335; c) F. Arcudi, L. Dordevic, M. Prato, *Acc. Chem. Res* **2019**, *52*, 2070.

[26] a) S. Liu, H. Yuan, H. Bai, P. Zhang, F. Lv, L. Liu, Z. Dai, J. Bao, S. Wang, *J. Am. Chem. Soc.* **2018**, *140*, 2284; b) L. Lin, Z. Su, Y. Li, C. Zhang, *Chemosphere* **2021**, *265*, 129060; c) L. Dordevic, F. Arcudi, M. Cacioppo, M. Prato, *Nat. Nanotechnol* **2022**, *17*, 112.

[27] a) Y. Song, S. Zhu, B. Yang, *RSC. Adv* **2014**, *4*, 27184; b) M. Li, C. Hu, C. Yu, S. Wang, P. Zhang, J. Qiu, *Carbon* **2015**, *91*, 291; c) S. Bhattacharyya, F. Ehrat, P. Urban, R. Teves, R. Wyrwich, M. Doblinger, J. Feldmann, A. S. Urban, J. K. Stolarczyk, *Nat. Commun* **2017**, *8*, 1401.

[28] a) S. Das, S. Mondal, D. Ghosh, *Front. Bioeng. Biotech.* **2024**, *11*, 1333752; b) X. Y. Xu, R. Ray, Y. L. Gu, H. J. Ploehn, L. Gearheart, K. Raker, W. A. Scrivens, *J. Am. Chem. Soc.* **2004**, *126*, 12736.

[29] Q. Quan, C. Fan, N. Pan, M. Zhu, T. Zhang, Z. Wang, Y. Dong, Y. Wu, M. Tang, X. Zhou, M. Chen, *Adv. Funct. Mater.* **2023**, *33*, 2303381.

[30] a) I. Noda, N. I. Afanas'eva, *Opt. Spectrosc.* **1997**, *83*, 52; b) I. Noda, *Appl. Spectrosc.* **1993**, *47*, 1329.

[31] C. Pang, G. Y. Lee, T. I. Kim, S. M. Kim, H. N. Kim, S. H. Ahn, K. Y. Suh, *Nat. Mater.* **2012**, *11*, 795.

[32] L. Yang, Z. Wang, H. Wang, B. Jin, C. Meng, X. Chen, R. Li, H. Wang, M. Xin, Z. Zhao, S. Guo, J. Wu, H. Cheng, *Adv. Mater.* **2023**, *35*, 2207742.

[33] Y. Zou, V. Raveendran, J. Chen, *Nano Energy* **2020**, *77*, 105303.

[34] H. Sun, Y. Zhao, S. Jiao, C. Wang, Y. Jia, K. Dai, G. Zheng, C. Liu, P. Wan, C. Shen, *Adv. Funct. Mater.* **2021**, *31*, 2101696.